

JGR Solid Earth

RESEARCH ARTICLE

10.1029/2021JB023321

Key Points:

- We are the first to image the critical zone using elastic full waveform inversion (EFWI) for P- (Vp) and S-wave (Vs) models
- We present practical EFWI strategies to reliably invert seismic refractions for Vp and Vs models with high-resolution structures
- Analysis of EFWI inverted Vp, Vs, Vp/Vs models can reveal three lithological layers and fluid properties of the critical zone

Supporting Information:

Supporting Information may be found in the online version of this article.

Correspondence to:

T. Zhu,
tyzhu@psu.edu

Citation:

Liu, X., Zhu, T., & Hayes, J. (2022). Critical zone structure by elastic full waveform inversion of seismic refractions in a sandstone catchment, central Pennsylvania, USA. *Journal of Geophysical Research: Solid Earth*, 127, e2021JB023321. <https://doi.org/10.1029/2021JB023321>

Received 27 SEP 2021
Accepted 14 FEB 2022

Critical Zone Structure by Elastic Full Waveform Inversion of Seismic Refractions in a Sandstone Catchment, Central Pennsylvania, USA

Xuejian Liu¹ , Tiejuan Zhu¹ , and Jordan Hayes² 

¹Department of Geosciences, The Pennsylvania State University, State College, PA, USA, ²Department of Earth Sciences, Dickinson College, Carlisle, PA, USA

Abstract Seismic imaging provides key information for revealing structures within Earth's critical zone (CZ) and quantifying subsurface fluid properties. The P-wave velocity (Vp) models estimated by seismic refraction tomography or acoustic full waveform inversion (FWI) are useful to delineate the thicknesses of weathered bedrock but ambiguously map fluid properties in CZ. Considering the complementary sensitivity of S-wave to subsurface fluid saturation, we explore advanced elastic full waveform inversion (EFWI) to estimate both Vp and S-wave velocity (Vs) models simultaneously. Several strategies are proposed for robust EFWI implementation of noisy single (vertical) component refraction data: (a) we window seismic data to preserve early arrivals mainly including P-wave, converted waves, and S-wave refractions; (b) we use a correlative misfit rather than the classic L_2 misfit to alleviate the interference of unreliable data amplitudes; and (c) we perform inversion using a multiscale frequency strategy with the iterative constraint with the rule of $Vp/Vs > 1$. We validate that the EFWI approach reliably reconstructs Vp and Vs models using synthetic data. Then, we apply our EFWI approach to seismic refraction data acquired at the Garner Run site of the Susquehanna Shale Hills Critical Zone Observatory. The inverted Vp and Vs models indicate three distinguished layers and with significant lateral and depth heterogeneities (e.g., low Vp and Vs zones). Joint analyses of Vp, Vs, and Vp/Vs with rock-physics knowledge reveal potential gas or water gathering zones.

Plain Language Summary The critical zone (CZ) is the permeable, heterogeneous near-surface layer of the Earth which manages gas exchange with atmosphere, filters water at surface and underground, and supports life at the surface. The near-surface heterogeneities and fluid (gas/water) properties are critical to understanding multiple CZ processes such as nutrient exchange and groundwater flow. To image near-surface heterogeneities, improve layer resolution, and characterize fluid properties in the CZ subsurface, we implement elastic full waveform inversion (EFWI) with single (vertical)-component seismic refraction data for estimating both P- (Vp) and S-wave velocity (Vs) models. We are able to interpret possible subsurface water flow paths and gas and water charged areas of CZ based on derived Vp, Vs, and Vp/Vs models.

1. Introduction

The critical zone (CZ) is the Earth's near-surface layer where rock, soil, water, air, and organisms interact with each other (National Research Council, 2001). These interactions include diverse atmospheric, hydrologic, geologic, and biologic processes that generate a relatively heterogeneous subsurface across the terrestrial landscape of Earth. The resulting near-surface heterogeneities from very top soil to bedrock are largely associated with fracturing or weathering effects of varied bedrock. On the other hand, near-surface heterogeneities will likely influence fluid distributions (e.g., surface water in upper soil layer and the deeper groundwater aquifers), thus influence CZ hydrologic processes and others. Characterizing near-surface heterogeneities and fluid distribution is therefore critical for understanding CZ processes (National Research Council, 2001; Parsekian et al., 2015).

Geophysical imaging is a cost-effective way to indirectly map variations in subsurface parameters within the CZ (e.g., seismic velocity, electrical resistivity, and dielectric permittivity) (Parsekian et al., 2015). As a primary geophysical imaging tool, seismic refraction tomography provides spatial P-wave velocity (Vp) models of the shallow subsurface by iteratively fitting picked first-arrival traveltimes. The tomographic Vp model can be used to quantify variations in thickness of weathered layers across the landscape (e.g., Befus et al., 2011; Flinchum et al., 2018; Ma et al., 2021). The Vp models can be further exploited by using rock-physics relationships to derive the porosity changes of the weathered layer (e.g., Hayes, Riebe, et al., 2019; Holbrook et al., 2014).

However, seismic refraction tomography is limited by its basis in ray theory that uses a high frequency assumption and can only produce long-wavelength, that is, low spatial resolution, velocity models (Sheng et al., 2006), which may result in ambiguous identification of lithological layers and poor delineation of near-surface heterogeneities (Holbrook et al., 2014; Parsekian et al., 2015). Moreover, ray-based refraction tomography will fail where isolated low-velocity zones (e.g., gas charged areas) exist since seismic rays bend away from low velocity zones (Virieux & Operto, 2009). Wang, Nyblade, et al. (2021) improved the accuracy of V_p models by applying wave-equation traveltimes tomography (WTT) to 3D CZ seismic datasets. The improvement is attributed to accurate theoretical traveltimes derived from synthetic seismograms by solving the wave equation, but their WTT still relies on traveltimes picking that is often difficult for near-surface refraction data where different arrivals are mixed and/or contaminated by ambient noise.

Compared to traveltimes-based inversion, full waveform inversion (FWI) of seismic data has been demonstrated to provide velocity models with higher spatial resolution by fitting whole seismic waveforms based on wave theory (Virieux & Operto, 2009). The initial concept of FWI was introduced by Lailly (1983) and Tarantola (1984, 1986). In recent years, the rapidly increasing computational power has enabled applications of FWI at different scales, including seismic exploration for imaging oil and gas reservoirs (Chi et al., 2015; Liu et al., 2018; Pan et al., 2016; Vigh et al., 2014; Virieux & Operto, 2009), crustal seismic imaging (Chen et al., 2007; Górszczyk et al., 2021; Kamei et al., 2012), global seismology for mantle structures (Bozdağ et al., 2016), and near-surface characterizations (Adamczyk et al., 2014; Wang et al., 2019).

For near-surface characterization, acoustic FWI is first applied to seismic refraction data by selecting early arrival waveforms (Adamczyk et al., 2014; Gao et al., 2006; Sheng et al., 2006; Smithyman et al., 2009), which can alleviate nonlinearities with much less local minima as compared to full data fitting. Recently, Huang et al. (2019) demonstrated that appropriate acoustic FWI on windowed refraction data is able to produce a detailed V_p model of CZ. However, we found that shear-wave refractions and converted waves are rich in the seismic refraction data (even in single [vertical]-component geophone data). Nevertheless, acoustic FWI cannot properly process shear waves and likely mistakes them as leakage P-waves to generate wrong updates with polarity and amplitude errors in the V_p model (Wang, Burtz, et al., 2021). To avoid this problem, elastic FWI (EFWI) is being more appropriately applied to seismic refractions with significant shear waves. More importantly, the enhanced ability of EFWI to generate both V_p and V_s models greatly improves rock physics translations for simultaneously quantifying subsurface porosity and fluid properties (Mavko et al., 2009). For instance, due to different sensitivity of P- and S-wave to fluid saturations (Mavko et al., 2009), joint analysis of V_p , V_s and V_p/V_s ratio can be useful for characterizing gas/liquid charged zones (Gu et al., 2020).

In this paper, we aim to design practical EFWI strategies to construct near-surface V_p and V_s models simultaneously. Considering the features of near-surface seismic data (vertical-component data, random noise, strong surface waves, and unreliable amplitudes, etc.), we first window out early arrival waveforms, mainly including first-arrival P-wave, converted wave, and S-wave refractions, to reduce nonlinearities for EFWI in real applications (Athanasopoulos et al., 2020; Sheng et al., 2006). Second, we use a correlative misfit to evaluate the closeness of global phase between the modeled and observed data with the normalized zero-lag cross-correlation function (Routh et al., 2011), and implement model regularization with an alternating Tikhonov and total variation (TV) penalty term (Gao & Huang, 2019; Lin & Huang, 2015; Modrak & Tromp, 2016) to improve the inversion stability and remove some inversion noise. We adopt this misfit to alleviate influences of complex nonlinear amplitude-versus-offset (AVO) variations of refraction data, especially when wave physics cannot be fully considered (e.g., unknown densities). Third, we implement multiscale frequency strategy (Bunks et al., 1995) to reduce the risks of cycle skipping at far offsets of refraction data, with an iterative constraint of $V_p/V_s > 1$ to reject nonphysical updates.

In numerical experiments, we first validate effectiveness and robustness of our EFWI approach with a series of synthetic experiments. Second, we apply EFWI to vertical-component refraction data acquired at the Garner Run site of Susquehanna Shale Hills Critical Zone Observatory (SSHCZO) in central Pennsylvania, USA (Del Vecchio et al., 2018; Li et al., 2018). Compared to ray-based tomographic V_p models, we successfully produce both V_p and V_s models with high-resolution details clearly delineating near-surface heterogeneities at the Garner Run site. With EFWI inverted V_p and V_s models, we distinguish CZ subsurface into three layers of colluvium/weathered rock, weathered/fractured bedrock, intact bedrock. By jointly analyzing the inverted V_p , V_s , and associated V_p/V_s with the fluid substitution, we indicate possible gas and water gathering zones at the Garner Run

site. We infer surface and underground water pathways by connecting high Vp/Vs zones which permeate into subsurface from the mountain hillslope, become underground water, and flow toward water aquifers around the valley.

2. Methodology

2.1. Theory of EFWI

Here, we briefly review the EFWI algorithm based on solving the first-order velocity-stress elastic-wave equation in isotropic elastic media. The wave equation is compactly written (Vigh et al., 2014) as

$$\begin{cases} \rho \frac{\partial \mathbf{v}}{\partial t} - E^T \sigma = 0, \\ \frac{\partial \sigma}{\partial t} - C E \mathbf{v} = \mathbf{s}, \end{cases} \quad (1)$$

where ρ represents the subsurface density, \mathbf{v} represents the particle velocity vector, σ represents the stress tensor, E represents the matrix of spatial differential operators, C represents the stiffness matrix (defined by Lamé moduli in isotropic elastic media), and \mathbf{s} represents the source function. We record the modeled data with multiple components as $\mathbf{d}_m = \mathbf{v}$ that propagate from the source position \mathbf{x}_s to the receiver position \mathbf{x}_r .

The standard EFWI is built by solving the classic least-squares optimization problem, that is, minimizing L_2 norm misfit of waveform differences between modeled and observed data, which relies on their direct amplitude differences. However, seismic modeling might not match observed data on amplitudes due to following reasons: amplitudes can be complex due to inconsistencies during seismic data acquisition (e.g., varied geophone response or coupling with the earth), seismic processing errors (e.g., improper utilization of automatic gain control), and/or varying source energies shot by shot. The aforementioned factors that directly impact amplitudes are not modeled by numerically solving elastic wave equation, and unreliable amplitudes in the observed data will be inverted as wrong subsurface structures. Hence, instead of a classic L_2 misfit employing exact amplitude matches (Virieux & Operto, 2009), we solve the correlative based misfit that measures the global phase closeness between the modeled data \mathbf{d}_m and the observed data \mathbf{d}_{obs} (Choi & Alkhalifah, 2012; Routh et al., 2011), as follows:

$$f(\mathbf{m}) = \int \int \left(1 - \frac{\int \mathbf{d}_m(\mathbf{x}_r, t; \mathbf{x}_s) \mathbf{d}_{obs}(\mathbf{x}_r, t; \mathbf{x}_s) dt}{\sqrt{\int \mathbf{d}_m^2(\mathbf{x}_r, t; \mathbf{x}_s) dt} \sqrt{\int \mathbf{d}_{obs}^2(\mathbf{x}_r, t; \mathbf{x}_s) dt}} \right) d\mathbf{x}_r d\mathbf{x}_s, \quad (2)$$

in order to reliably invert elastic model parameters \mathbf{m} . If the product $N_r * N_s$ counts the number of total seismic traces, the misfit is normalized as $\frac{f(\mathbf{m})}{N_r * N_s}$. We will measure waveform matches using the normalized misfit in numerical results and indicate it as “DCC” for conveniently describing the “de-crosscorrelation” measurement. The correlative misfit relaxing the offset- and shot-dependent amplitude matches can makes EFWI of refraction data more robust than a classic L_2 misfit.

To calculate the adjoint wavefields in isotropic elastic media, we use the same wave equation system as Equation 1 but replace the point source term with adjoint sources, written as

$$\begin{cases} \rho \frac{\partial \tilde{\mathbf{v}}}{\partial t} - E^T \tilde{\sigma} = \frac{\partial f(\mathbf{m})}{\partial \mathbf{d}_m}, \\ \frac{\partial \tilde{\sigma}}{\partial t} - C E \tilde{\mathbf{v}} = \mathbf{0}, \end{cases} \quad (3)$$

where we use the head tilde to denote adjoint wavefields. We solve this Equation 3 in the reverse time to backward propagate the adjoint wavefields.

Following the explicit expression of gradients with respect to stiffness elements and the density given by Vigh et al. (2014), we write the gradients for 2D isotropic elastic media as

$$\left\{ \begin{array}{l} \frac{\partial f(\mathbf{m})}{\partial \lambda} = -f \left(\left(\begin{array}{ccc} 1 & 1 & 0 \\ 1 & 1 & 0 \\ 0 & 0 & 0 \end{array} \right) \left(\mathbf{C}^{-1} \frac{\partial}{\partial t} \sigma \right) \right)^T (\mathbf{C}^{-1} \tilde{\sigma}) dt, \\ \frac{\partial f(\mathbf{m})}{\partial \mu} = -f \left(\left(\begin{array}{ccc} 2 & 0 & 0 \\ 0 & 2 & 0 \\ 0 & 0 & 1 \end{array} \right) \left(\mathbf{C}^{-1} \frac{\partial}{\partial t} \sigma \right) \right)^T (\mathbf{C}^{-1} \tilde{\sigma}) dt, \\ \frac{\partial f(\mathbf{m})}{\partial \rho} = f \left(\frac{\partial}{\partial t} \mathbf{v} \right)^T \tilde{\mathbf{v}} dt, \end{array} \right. \quad (4)$$

where λ and μ are Lamé moduli. However, inversion with Lamé moduli parameterization often faces inter-parameter cross-talk artifacts (Köhn et al., 2012). To suppress this type of artifacts, we will further formulate parameterization for direct inversion of seismic velocities (Köhn et al., 2012; Vigh et al., 2014).

Moreover, we need to avoid the density inversion (Vigh et al., 2014) in our practice with two-fold reasons: except the density inversion is essentially ambiguous (Köhn et al., 2012), the windowed refraction data lack small scattering-angle energies that are required for reconstructing density according to its radiation pattern (Virieux & Operto, 2009); besides, density inversion tends to be unreliable in real applications as seismic amplitudes of field data are influenced by various factors, that is, density, reflectivity, seismic attenuation, and source-receiver coupling effect, and data processing.

Therefore, we use the correlative misfit with normalized amplitude match criteria to focus on inverting Vp and Vs models, with the assumption of a constant density model ρ_0 . With the following relationships:

$$\begin{aligned} \lambda &= \rho_0 v_p^2 - 2\rho_0 v_s^2, \\ \mu &= \rho_0 v_s^2, \end{aligned} \quad (5)$$

we can construct gradients for Vp and Vs inversion using the chain rule as

$$\begin{aligned} \frac{\partial f(\mathbf{m})}{\partial v_p} &= \frac{\partial f(\mathbf{m})}{\partial \lambda} \frac{\partial \lambda}{\partial v_p} = 2\rho_0 v_p \frac{\partial f(\mathbf{m})}{\partial \lambda}, \\ \frac{\partial f(\mathbf{m})}{\partial v_s} &= \frac{\partial f(\mathbf{m})}{\partial \lambda} \frac{\partial \lambda}{\partial v_s} + \frac{\partial f(\mathbf{m})}{\partial \mu} \frac{\partial \mu}{\partial v_s} \\ &= -4\rho_0 v_s \frac{\partial f(\mathbf{m})}{\partial \lambda} + 2\rho_0 v_s \frac{\partial f(\mathbf{m})}{\partial \mu}, \end{aligned} \quad (6)$$

where \mathbf{m} specifically indicates $[v_p v_s]$. Then, a basic EFWI algorithm can be built with any gradient-based inversion method (Nocedal & Wright, 2006).

In order to stabilize the inverted models and make the inversion procedure more robust, we introduce hybrid Tikhonov and total-variation (TV) based regularization terms. Then, we solve the regularized misfit by alternately minimizing the following two optimal problems:

$$\mathbf{m}^{(i)} = \underset{\mathbf{m}}{\operatorname{argmin}} \left\{ f(\mathbf{m}) + \frac{\varepsilon_1}{2} \left\| \mathbf{m} - \mathbf{u}^{(i-1)} \right\|_2^2 \right\}, \quad (7)$$

and

$$\mathbf{u}^{(i)} = \underset{\mathbf{u}}{\operatorname{argmin}} \left\{ \left\| \mathbf{m}^{(i)} - \mathbf{u} \right\|_2^2 + \varepsilon_2 \left\| \mathbf{u} \right\|_{TV} \right\}, \quad (8)$$

where the superscript i represents the iteration number, \mathbf{u} denotes TV de-noised auxiliary models with an initial guess of $\mathbf{u}^{(0)} = \mathbf{m}^{(0)}$, and ε_1 and ε_2 are regularization weighting coefficients.

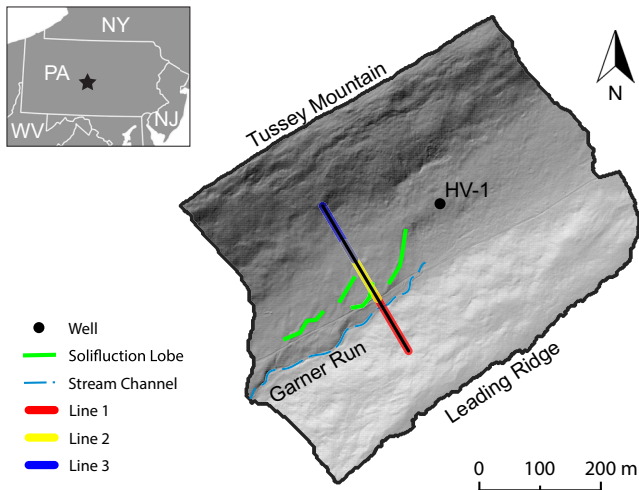


Figure 1. A hillside digital elevation map of the Garner Run subcatchment with labeled positions of three overlapped seismic acquisition lines. The water stream flows through valley and rocky colluvium fill topography surface due to solifluction effects (Del Vecchio et al., 2018; Li et al., 2018). The HV-1 well was drilled approximately 200 m from acquisition lines, which shows colluvial fill to approximately 9 m depth.

Equation 7 presents a conventional Tikhonov constrained optimal problem, for which the gradient can be easily constructed by adding Equation 6 with the derivative of the Tikhonov term. Equation 8 presents an imaging de-noising problem, which is efficiently solved with the split-Bregman iteration method (Goldstein & Osher, 2009) and can be generalized by incorporating a second-order derivative term of velocity models (Gao & Huang, 2019). The de-noised model \mathbf{u} by Equation 8 serves as prior information in the Tikhonov term of Equation 7. At each iteration of multi-scale frequency procedure, we solve Equation 7 with the standard L-BFGS method (Nocedal & Wright, 2006) for velocity inversion. This regularization term can preserve sharp interfaces while suppressing random artifacts typically due to noisy data or aliased data sampling (Gao & Huang, 2019; Lin & Huang, 2015).

In addition, due to data noise, not fully accounted physics for wave propagations in the application of field data, the uncertainties of elastic velocity inversion (Huang & Zhu, 2020; Liu & Peter, 2020), etc., there may be updates of V_p and V_s with unreasonable V_p/V_s values in applications with field data. Here we design an automated procedure to reject the possible unreasonable velocity updates by introducing additional constraint $V_p/V_s > 1$ at each iteration of multiscale frequency procedure (see details in Text S1 in Supporting Information S1).

2.2. Qualitative Analysis of V_p/V_s With Water/Gas Saturation

In order to qualitatively interpret subsurface fluid properties from the EFWI V_p/V_s result, we first need to understand how V_p , V_s , and V_p/V_s models change with varied fluid properties using the rock-physics theory (see details in Supporting Information S1). We summarize the water/gas (air) substitution effects as follows: (a) water filling effect—with increased water saturation and decreased gas saturation, V_p increases because the bulk modulus increases, V_s decreases because the shear modulus does not change but the bulk density increases; thus, V_p/V_s increases (Mavko et al., 2009); on the contrast, (b) gas filling effect—with increased gas saturation and decreased water saturation, V_p decreases, V_s increases, and V_p/V_s decreases, (c) V_p/V_s is most sensitive to fluid substitution as V_p and V_s have opposite fluid effects as above described.

3. Experiments and Results

Our field seismic data sets were acquired in the Valley and Ridge province of central Pennsylvania along synclinal valley topography at Garner Run field site of SSHCZO (Hayes, 2019), which is a subcatchment underlain by subsurface sandstones (Del Vecchio et al., 2018; Li et al., 2018). A hillshade map with seismic survey locations is presented in Figure 1. There are a total of 74 sledge-hammer shots with a uniform space of 8 m collected over three seismic arrays (Line 1, Line 2, and Line 3) each with 48 vertical geophones uniformly spaced at 4 m. Only vertical components (V_z) seismic data were recorded at surface.

We preprocess the windowed seismic data as displayed in Figure 2 with the following steps: filtering seismic data using a low-pass frequency filter with the sine-squared taper range of 80–120 Hz to reject high-frequency noises; estimating a source wavelet from selected first-arrival waves; amplitude corrections by scaling seismic data with the square root of time to account for 3D to 2D conversion (Ravasi et al., 2015); removing strong surface waves, and preserving early-arrival waveforms mainly containing P, PS, and S refractions for velocity inversion. Since all surface waves have been muted out and will not be included, we circumvent the complex free-surface simulation along rugged topography. We extend the first-layer velocities along topography into the air layer, and set the absorbing boundary layer at the flat top of the computational model.

Before applying our EFWI method and strategies to real data, we generate synthetic data sets for validation experiments. In Subsection 3.1, we first validate that, with refractions of a single-component V_z , EFWI can effectively

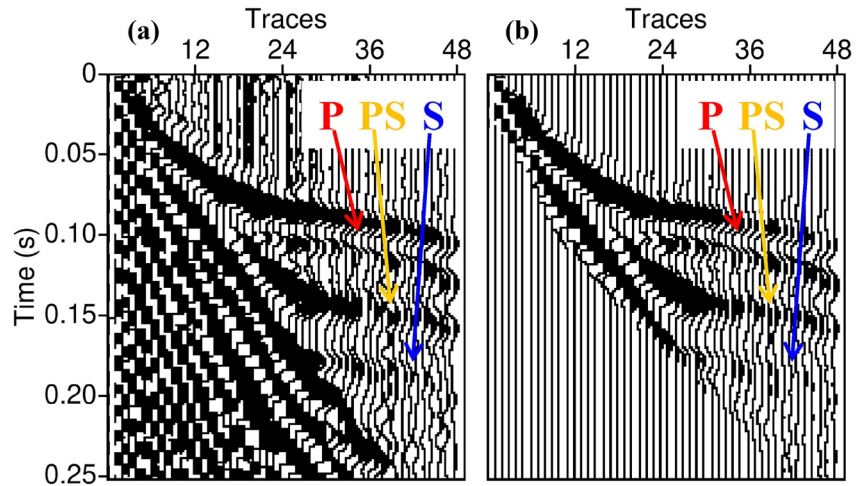


Figure 2. (a) An example of raw seismic data with only the vertical components acquired at the Garner Run site, and (b) the processed refraction data. The P-wave, PS-wave, and S-wave refractions are labeled.

invert for satisfied V_p and V_s models using a L_2 or correlative misfit (Test 1 and 2). Then, we verify the robustness of the regularized correlative misfit in EFWI when observed amplitudes of seismic refractions cannot be accurately modeled by elastic wave equation with unknown densities (Test 3–5).

3.1. Synthetic Validation of EFWI Strategies

We design synthetic V_p and V_s models, as shown in Figure 3, with same acquisition geometry and topography as the Garner Run case. The V_s model is generated through dividing V_p by $\sqrt{3}$. The models are spaced with a grid interval of 1 m.

We use the time-domain finite-difference waveform modeling of 2nd-order temporal and 16th-order spatial accuracy with a 50-Hz Ricker wavelet to synthesize seismic data, and then we window out the early-arrival waveforms of V_z before velocity inversion. Figure 4 shows an example of synthetic data gather with labeled P, PS, and S refractions. We have synthesized the first data set with a constant density ($1,000 \text{ kg/m}^3$) as shown in Figure 4a. We make a density model with the Gardner's relation (Gardner et al., 1974): $\rho = 310 \times V_p^{0.25}$, and have synthesized the second data set with varied densities as shown in Figure 4b, the amplitude differences of which are significant as shown in Figure 4c.

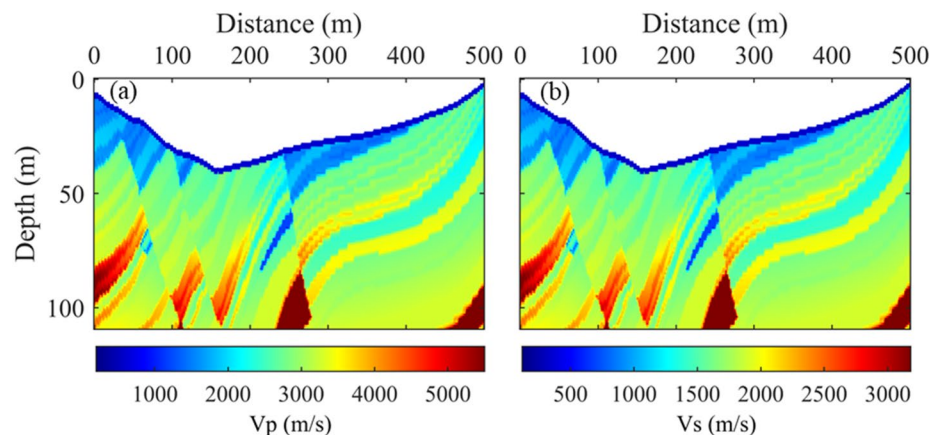


Figure 3. Synthetic (a) V_p and (b) V_s models for validating the effectiveness and robustness of our EFWI strategies. The model geometry and topography are derived from the Garner Run site.

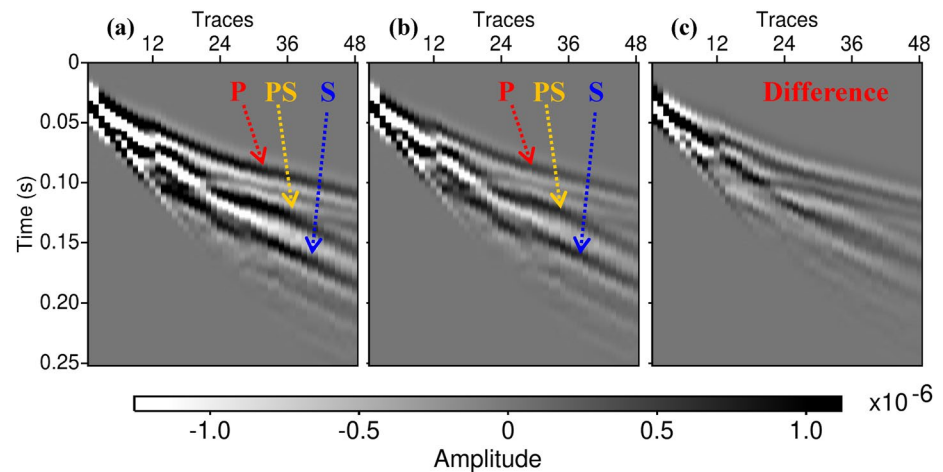


Figure 4. Vertical-component seismic data gathers are (a) synthesized with V_p and V_s models and a constant density and (b) synthesized using varied densities derived from Gardner's relation. (c) The data difference is produced by subtracting the data in panel (a) from that in panel (b).

The first test (Test 1 in Figure 5) shows that, with refractions of a single-component V_z , EFWI with the classic L_2 misfit can invert for detailed V_p and V_s models. The initial V_p model is computed by matching first-arrival traveltimes with ray-based seismic tomography. Then we estimate the initial V_s model through dividing the initial V_p by $\sqrt{3}$. Initial V_p and V_s models are presented in Figures 5a and 5b, respectively. At first, we perform EFWI with the classic L_2 misfit, which converges well with the final misfit as 0.63%. The inverted V_p and V_s models, displayed in Figures 5c and 5d, respectively, present much more detailed subsurface structures with located low velocity zones relative to initial models. We confirm that it is viable to use early-arrival waveforms of V_z for both V_p and V_s inversion, although we observe some losses of velocity details as compared to inversion with complete multi-component data in our tests.

In the second test (Test 2 in Figure 5), will show that EFWI with the correlative misfit provides better updates with more subsurface details. As shown in Figures 5e and 5f, improved velocity updates in the deep parts relative to results with the L_2 misfit are indicated by arrows. The reason is that the near offsets with higher amplitudes relatively dominate the measurement of L_2 misfit, whereas the correlative misfit has the advantage of balancing contributions between near and far offsets of windowed refraction data.

We then test the robustness of the regularized correlative misfit in EFWI when seismic refractions are modeled with incomplete propagation physics, that is, unknown densities. The second data set synthesized with varied densities, as shown in Figure 4b, is used for velocity inversion, and results are shown in Figure 6 (Tests 3–5). Here, we still start from initial velocity models as displayed in Figures 5a and 5b, and assume that the density is unknown during seismic inversion as discussed in the theory part (between Equations 4 and 5). We first test EFWI with the L_2 misfit, which, however, fails to converge and provides poor velocity updates as displayed in Figures 6a and 6b (Test 3). Second, we test EFWI with the correlative misfit, which works well and provides detailed velocity updates as displayed in Figures 6c and 6d (Test 4). This test validates that the correlative misfit is robust to invert elastic refraction data for velocities in case of unknown densities. However, the inaccurate modeling still introduces additional random noise. Third, we try to improve the inversion with the alternating Tikhonov and TV-based regularization term. The results are displayed in Figures 6e and 6f (Test 5), which show reduced noise relative to results in Figures 6c and 6d as indicated by arrows and dashed ellipses.

Data matches for all five tests in Figures 5 and 6 are gathered in Figure 7. Not surprisingly, Figures 7a and 7d show poor matches with the initial tomographic velocity models. The comparisons among Figures 7b–7g demonstrate that the correlative misfit improves far-offset data matching. Comparing Figures 7c and 7f with Figures 7b and 7e, respectively, indicates the failure of the inversion with the L_2 misfit in case of unknown densities; however, the comparison between Figures 7g and 7h shows that the inversion with the correlative misfit is barely influenced by unknown densities. We conclude that application of the correlative misfit to windowed refraction data is robust in solving amplitude problems including incomplete propagation physics such as unknown densities. The physics behind this is that the correlative misfit measures the global phase match along time and early-arrival

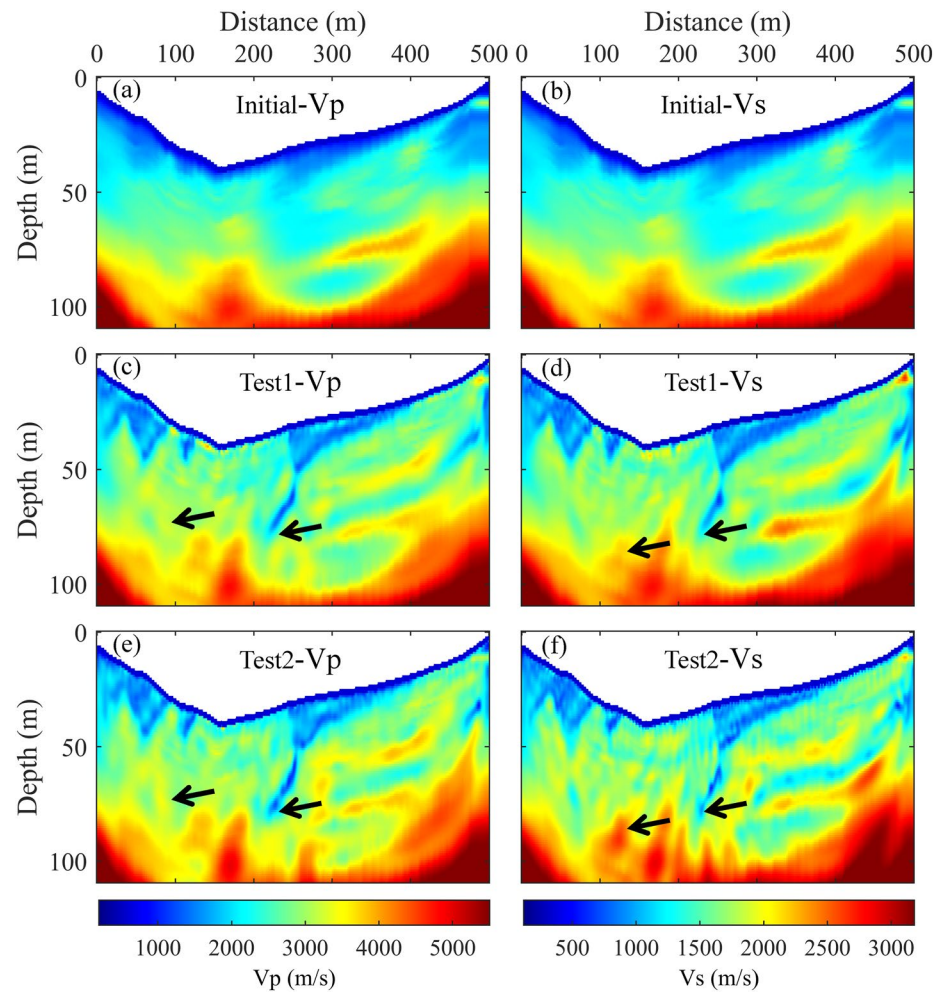


Figure 5. Seismic data synthesized with a constant density as shown in Figure 4a are used for Vp and Vs inversion. (a) The initial Vp model by seismic refraction tomography. (b) The initial Vs model is empirically converted from Vp. The inverted (c) Vp and (d) Vs models by EFWI with the L_2 misfit. The inverted (e) Vp and (f) Vs models by EFWI with the correlative misfit. As indicated by arrows, more velocity details in deep parts are inverted with the correlative misfit.

windowing makes it more robust by reducing complexities along time relative to complete data. Furthermore, the hybrid regularization term has been proven to remove random noise from inverted velocities, which also promotes data matches here as shown by the comparison between Figures 7h and 7i. In this experiment, we have validated that our EFWI method with regularized correlative misfit is practical and robust when applied to elastic refraction data of windowed Vz components for recovering shallow subsurface structures. In addition, we solve the regularized misfit using the multiscale strategy with progressive low-pass frequency groups (0–30, 0–60, and 0–120 Hz). Then, we further demonstrate the practical applicability of the same EFWI method and frequency choice to another synthetic test with Vp/Vs anomalies and the actual field data collected at the Garner Run site.

3.2. Synthetic Validation of Varying Vp/Vs Anomalies

We design synthetic Vp and Vs models with varying Vp/Vs anomalies, as shown in Figures 8a and 8b to test whether the proposed EFWI can reconstruct varying Vp/Vs anomalies as well as suppress cross-talks between Vp and Vs. Locally low Vp and Vs zones are added at different horizontal and depth positions, which accounts for low and high Vp/Vs anomalies, respectively. We use a 50-Hz Ricker wavelet to simulate seismic data, and then we window out the early-arrival refractions of vertical component particle velocity data Vz for EFWI.

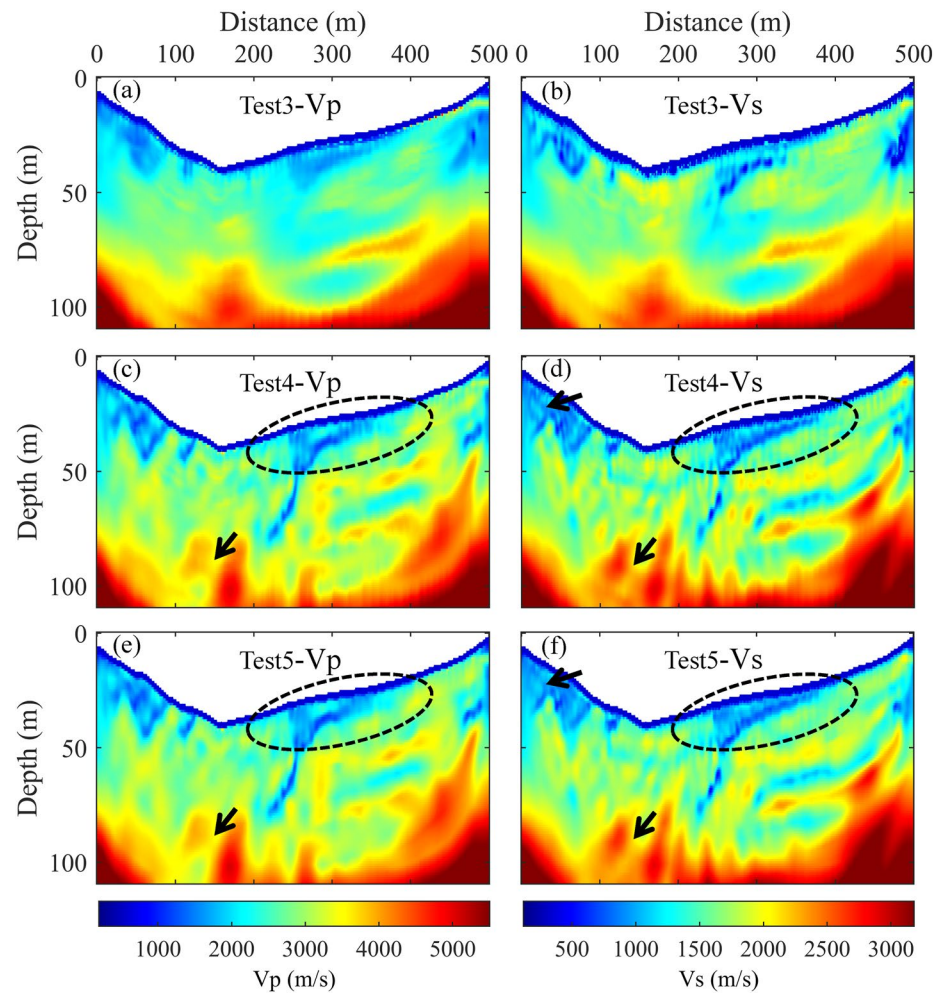


Figure 6. Seismic data synthesized with varied densities as shown in Figure 4b are used for Vp and Vs inversion. The inverted (a) Vp and (b) Vs models with the L_2 misfit, the inverted (c) Vp and (d) Vs models with the correlative misfit, and the inverted (e) Vp and (f) Vs models with the regularized correlative misfit. Some random noise has been removed by regularizations as indicated by the dashed ellipses and arrows.

The background Vp and Vs models excluding those low velocity anomalies are shown in Figures 8c and 8d, with a Vp/Vs ratio of $\sqrt{3}$. The maximum low Vp and Vs perturbations in Figures 8a and 8b reach about 27% and 43% of background Vp and Vs, respectively. Starting from these background Vp and Vs models, we apply our proposed EFWI method with regularized correlative misfit to windowed Vz refraction data using three low-pass frequency groups (0–30, 0–60, and 0–120 Hz). We successfully reconstruct the Vp and Vs models with recovered low velocity zones as shown in Figures 8e and 8f. Furthermore, the inverted Vp/Vs anomalies in Figure 8h are very close to true ones in Figure 8g with only 1.08% errors.

From this experiment, we find that the well-recovered Vp/Vs model is not dependent on initial Vp/Vs. The finding also illustrates that our EFWI strategies of refraction data are not challenged by cross-talks between Vp and Vs, for two reasons: (a) from theoretical radiation pattern analysis (Prioux et al., 2013b), only P waves with intermediate diffraction/reflection angle can produce limited cross-talks between Vp and Vs, but the windowed refractions are considered large angle information dominant; (b) L-BFGS algorithm, approximately accounting for the inverse of the Hessian preconditioning, mostly mitigates inter-parameter cross-talks (Prioux et al., 2013a, 2013b).

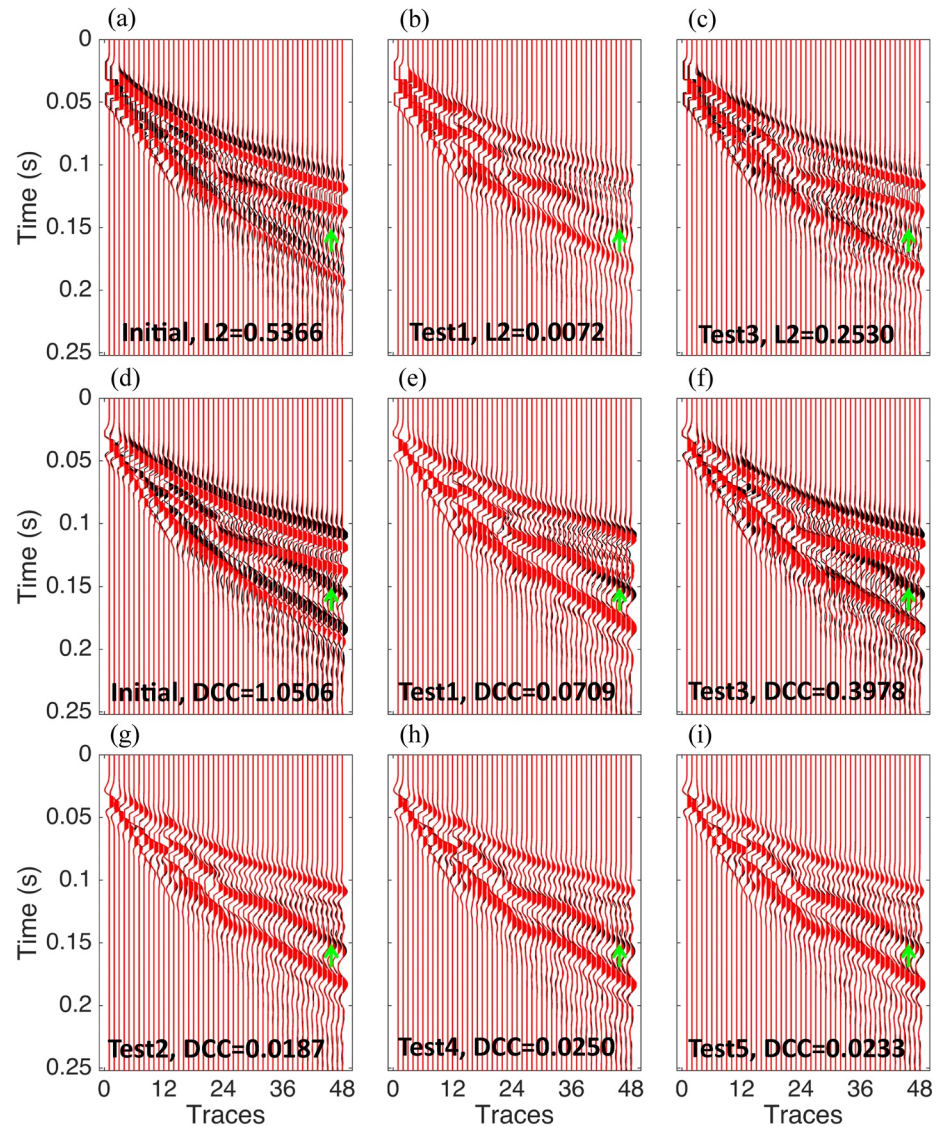


Figure 7. Data matches for synthetic tests in Figures 5 and 6 are measured with the standard “L2” (square of data differences) and “DCC” (Equation 2). Black and red wiggles stand for observed and synthetic data, respectively. Data matches for (a) initial velocities, (b) test1, and (c) test3 are measured with “L2,” which are balanced by the corresponding trace amplitude and replotted in (d), (e), and (f) with the “DCC” measurement, respectively. Data matches for (g) test2, (h) test4, and (i) test5 with “DCC.” The green arrows indicate that correlative misfits provide better data matches at far offsets.

3.3. Application of EFWI to Garner Run Field Data

The initial V_p model as displayed in Figure 9a is inverted by first-arrival seismic refraction tomography, and the initial V_s model as displayed in Figure 9b is empirically converted through dividing the V_p model by $\sqrt{3}$, where the models are discretized with a grid interval of 1 m. Shots and receiver arrays are labeled in Figures 9a and 9b, respectively, where three acquisition lines are depicted with red, yellow, and magenta colors, respectively. Note that we have excluded left- and right-hand bottom corner areas from plotting, where source wavefields scarcely reach according to source-illumination analysis and there will have no reliable velocity updates. In the implementation of EFWI of field data, we select three sequential frequency groups (0–30, 0–60, and 0–120 Hz). We avoid unreasonable velocity updates by imposing the limitation of $V_p/V_s > 1$ and adjusting V_p and V_s perturbations with weighting factors as described in Text S1 in Supporting Information S1.

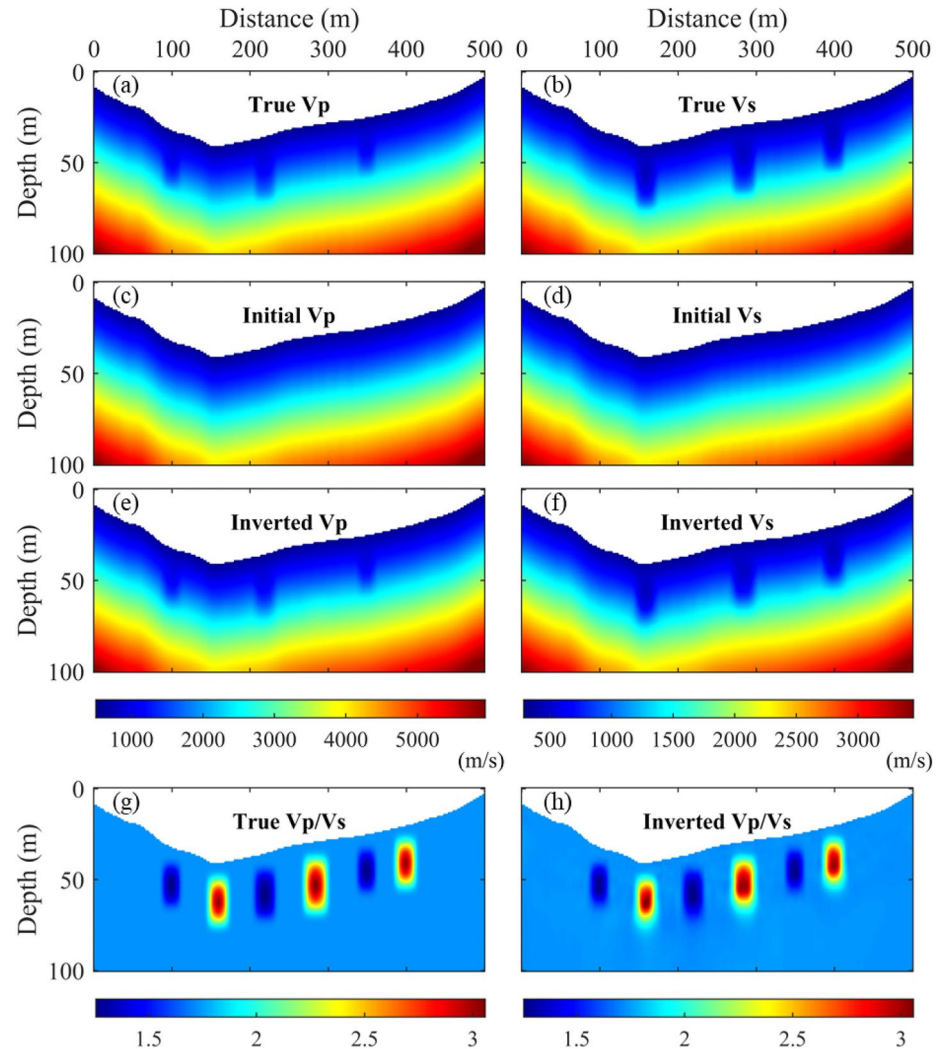


Figure 8. The true (a) V_p and (b) V_s models, where low V_p zones are placed at different positions from low V_s zones. Using the initial (c) V_p and (d) V_s models with a fixed V_p/V_s , the proposed EFWI is able to build (e) V_p and (f) V_s models with recovered low velocity zones. (h) The inverted V_p/V_s result is close to the true (g) V_p/V_s model.

The inverted V_p and V_s model by EFWI are shown in Figures 9c and 9d, respectively. From our EFWI inverted velocity models in Figures 9c and 9d, V_p values increase from about 500 m/s at the surface to >4,000 m/s at depth and V_s values increase from about 300 m/s at the surface to >2,500 m/s at depth. Compared to initial ray-based tomographic V_p and V_s models, our EFWI results clearly present structural details with lateral and vertical heterogeneities, as depicted by variations of velocity contours. Especially, low velocity zones are captured as indicated by arrows. As pointed by white arrows in Figures 9a and 9c, EFWI captures local low V_p zones under the valley and at the northwest (NW) Tussey Mountain hillslope. As pointed by black arrows in Figures 9b and 9d, similarly, the V_s structure in Figure 9d presents low velocity zones at similar horizontal distances but deeper depths relative to the inverted V_p in Figure 9c. Under the valley, the V_s structure (the left-most arrow in Figure 9d) extends from deep to the shallow surface (approximately 5 m below topography).

We further compare three 1D depth profiles from initial models and EFWI inverted models, as shown in Figure 10. The initial 1D velocity profiles (dashed lines) show nearly linear increased velocities with depths, whereas 1D EFWI velocity profiles (solid lines) present depth and gradient variations, especially within 30 m below surface. Clearly, the low velocity zone at depths 10–20 m at the distance 120 and 165 m is overestimated in the initial

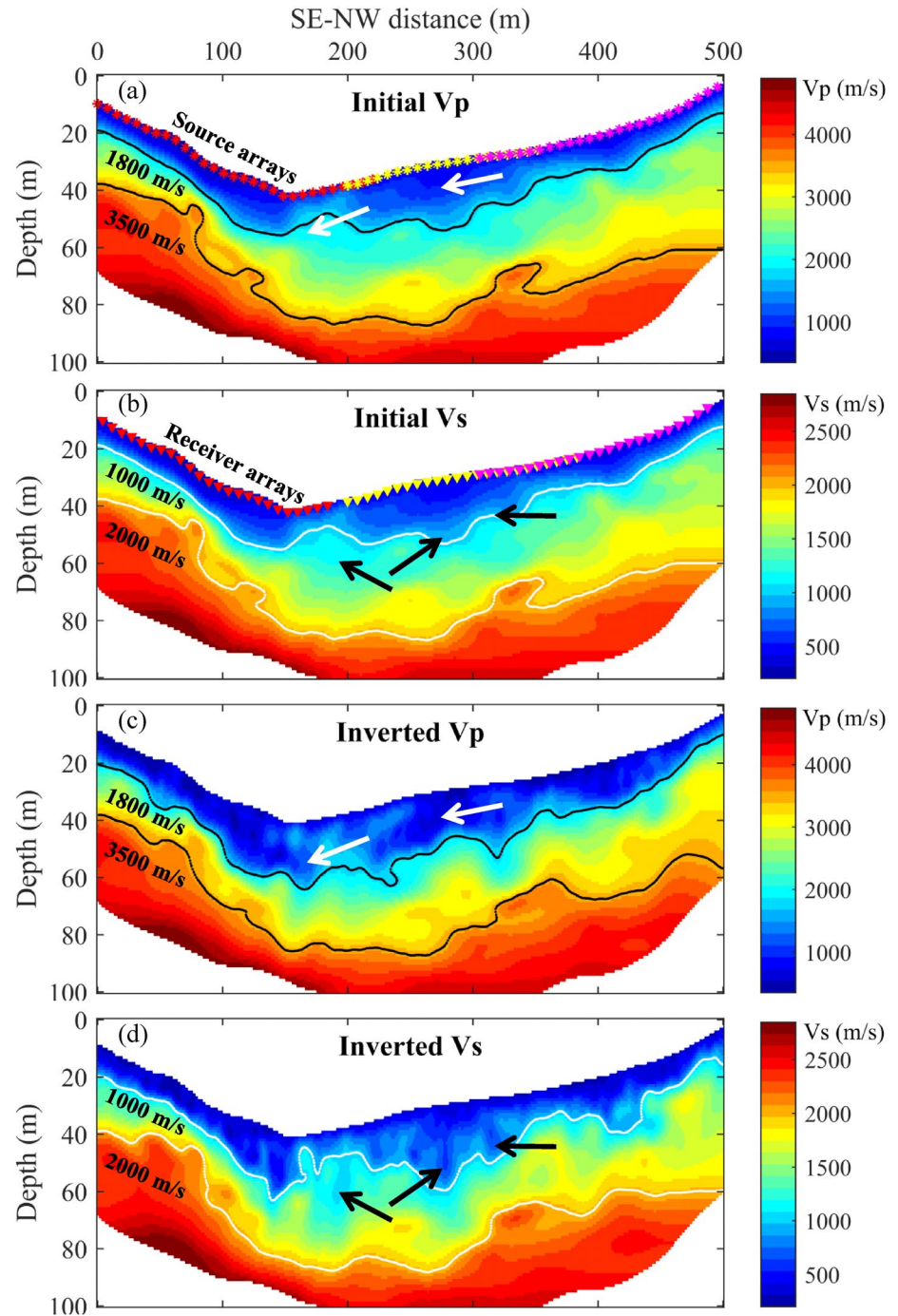


Figure 9. (a) V_p and (b) V_s models from ray-based refraction tomography that are used as initial input for EFWI. The inverted (c) V_p and (d) V_s models using EFWI with the regularized correlative misfit. Arrows and velocity contours label detailed updates by EFWI.

V_p and V_s . At 277 m, the decrease to increase of V_p from shallow to deep is clearly illustrated by the EFWI 1D profile, and the low V_s velocity zone between 15 and 30 m is enhanced in the EFWI 1D V_s profile.

To evaluate the performance of inversion, we compare the modeled waveforms with initial and final models (Figure 9) to observed waveforms in Figure 11. We pick one shot gather from each source-receiver array for waveform comparisons, and the observed and modeled data are plotted with black and red wiggles, respectively. Using initial models from refraction tomography, the first-arrival P waveforms (first peak-trough) are roughly matched

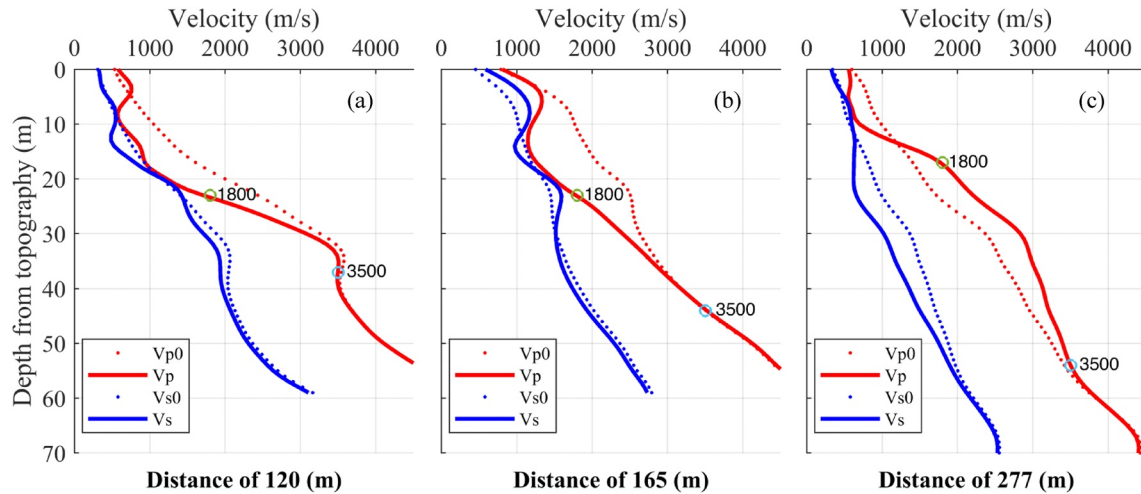


Figure 10. The 1D depth plots at the distance of (a) 120 m, (b) 165 m, and (c) 277 m are displayed, where ray-based tomographic initial and EFWI inverted Vp and Vs are plotted with dashed and solid line, respectively. The initial 1D profiles give the smoothed and linear increase velocity trend, whereas EFWI 1D profiles capture clear velocity depth variations in Vp and Vs, especially within 30 m below the surface. Furthermore, we will use the Vp contours of 1,800 and 3,500 m/s as labeled here to roughly divide subsurface into three layers.

but later arrivals are deviated (Figures 11a–11c). Using the EFWI updated models, the modeled data show much better matches with the real data at both P and later S waveforms for all three shot records (Figures 11d–11f). Better waveform matching is also reflected by the waveform correlation values at the bottom of Figures 11d–11f. Improved waveform matching demonstrates that our EFWI inversion strategies can effectively update both Vp and Vs velocities along the topography.

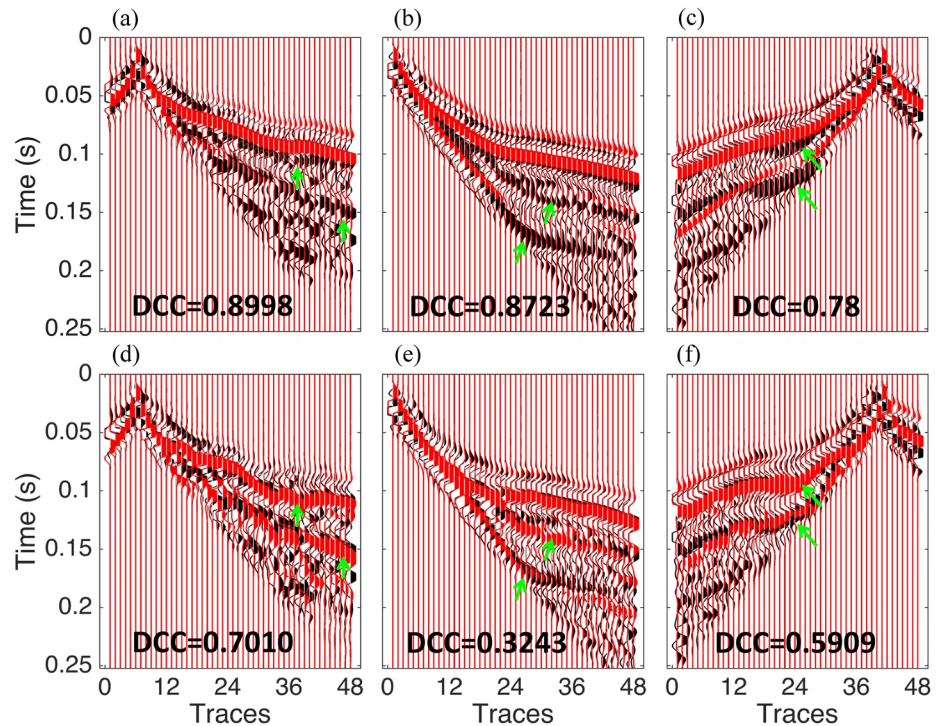


Figure 11. Waveform comparisons before EFWI are plotted for shots at the distance of (a) 24 m, (b) 200 m, and (c) 465 m of the model, and they are displayed after EFWI in (d), (e), and (f), respectively, where black and red wiggles stand for observed and synthetic data, respectively. These comparisons are measured with the standard “DCC” (normalized misfit in Equation 2). Green arrows indicate great improvements of data matches after EFWI. Here the source wavelet for seismic modeling is presented in Figure S1 in Supporting Information S1.

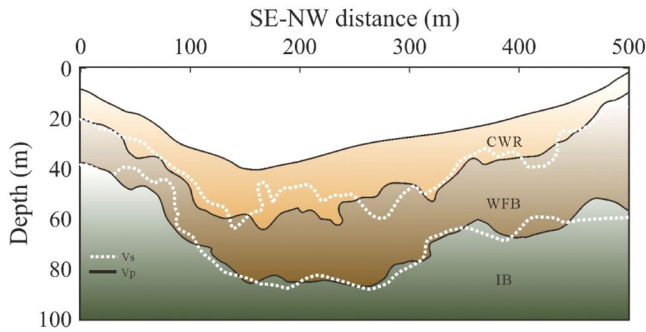


Figure 12. An interpreted model with three stratigraphic layers of colluvium/ weathered rock (CWR), weathered/fractured bedrock (WFB), and intact bedrock (IB). The three layers are divided primarily based on V_p contours of 1,800 and 3,500 m/s as shown in Figure 9c. The V_s contours of 1,000 and 2,000 m/s as shown in Figure 9d are plotted using dashed white lines as references.

(Del Vecchio et al., 2018). Specifically, the presence of solifluction lobes, more abundant boulder cover, and thicker colluvium are observed along the Tussey Mountain hillslope (NW portion) is consistent with thicker regions of lower seismic velocities. Further support to this interpretation is direct observations from the HV-1 well drilled approximately 200 m from this line showing colluvial fill to approximately 9 m depth (Del Vecchio et al., 2018; Li et al., 2018). However, it should be noted that this seismic profile does not extend the full length of the hillslopes to the ridgetops and therefore further surveying should be done to better constrain these subsurface aspect variations.

3.4. Interpretation of CZ Structure and Fluid Distribution

In this section, we first correlate the velocities (V_p and V_s) by EFWI to three divided layers. Then we identify the fluid properties from the joint analyses of V_p , V_s , and V_p/V_s . Finally, we propose a conceptual model combining three divided layers with inferred water flow paths.

According to previous studies (Del Vecchio et al., 2018; Gu et al., 2020), we identify three zones in the profile, as shown in Figure 12. The uppermost layer ($V_p < 1,800$ m/s and $V_s < 1,000$ m/s) shows lateral velocity variations from SE to NW. This layer is attributed to mixing of thin soils and rocky colluvium filling, which is consistent with field observations at this site (Del Vecchio et al., 2018; Li et al., 2018) due to solifluction effect as indicated in Figure 1. This colluvium/weathered rock layer under the valley extends to approximately 20 m below the surface, which is relatively thicker in the valley and the NW Tussey Mountain hillslope (approximately 10–20 m) compared to that along the SE Leading Ridge hillslope (approximately 10 m). This is consistent with field observations of regolith asymmetry attributed to periglacial climates during the Last Glacial Maximum and/or variations in slope

(Del Vecchio et al., 2018). Specifically, the presence of solifluction lobes, more abundant boulder cover, and thicker colluvium are observed along the Tussey Mountain hillslope (NW portion) is consistent with thicker regions of lower seismic velocities. Further support to this interpretation is direct observations from the HV-1 well drilled approximately 200 m from this line showing colluvial fill to approximately 9 m depth (Del Vecchio et al., 2018; Li et al., 2018). However, it should be noted that this seismic profile does not extend the full length of the hillslopes to the ridgetops and therefore further surveying should be done to better constrain these subsurface aspect variations.

The second layer ($1,800 < V_p < 3,500$ m/s) shows heterogeneities in both lateral and depth directions. This layer of intermediate velocities is referred to as weathered/fractured bedrock and we interpret to represent fractured sandstone, larger water saturation, and/or highly compacted colluvium. This layer represents a transition in the velocity depth profile from lower velocities toward consistent higher velocities. As depicted in Figure 10, roughly below the contour of $V_p = 1,800$ m/s, V_p increase quickly corresponding to large V_p/V_s , when $V_p = 3,500$ m/s seems to be another transition point toward the deepest layer. The deepest layer we interpret as intact and relatively unweathered bedrock where V_p values are in the range of 3,500–4,900 m/s. We define $V_p = 3,500$ m/s (with $V_s = 2,000$ m/s as a reference) to separate the bedrock layer. Overall, the interfaces from V_p and V_s contours in Figure 12 show similar depth and lateral locations. The discrepancies of V_p and V_s contours, in particular along the valley floor, may be caused by their different sensitivities to fluid (gas/water) accumulation in the CZ.

Then, we use joint analyses of V_p , V_s , and V_p/V_s ratio to identify possible fluid zones. Figure 13a shows the plot of V_p/V_s with the range of (1, 3.5). Some V_p/V_s values can be low to one, which are the possible indication of rock anisotropy which could cause very low V_p/V_s ratios (Wang et al., 2012). We highlight low V_p/V_s zones in Figure 13a (see white arrows), corresponding to low V_p zones in Figure 9c. The black arrows point to high V_p/V_s zones in Figure 13a, corresponding to low V_s zones in Figure 9d. As our analysis is shown in Section 2.2, water effects result in increased V_p , decreased V_s , and increased V_p/V_s , whereas gas (air) effects oppositely show decreased V_p , increased V_s , and decreased V_p/V_s . Therefore, the high V_p/V_s but low V_s zones where black arrows indicate in Figures 9d and 13a

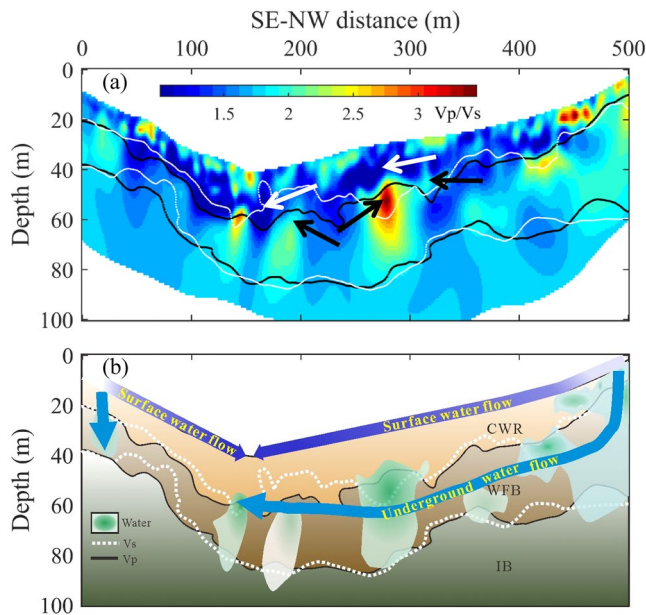


Figure 13. (a) The plot of V_p/V_s derived from final models in Figures 9c and 9d. White color arrows point to low V_p/V_s values here, and point to low V_p values in Figure 9c, which jointly reveals gas (air) charged zones. Black color arrows point to high V_p/V_s values here, and point to low V_s values in Figure 9d, which jointly indicates the water-charged areas. The three-layer boundaries determined by V_p and V_s contours are attached as black and white lines, respectively. (b) An interpretive conceptual model combining the three layers with the inferred water flows and possible water aquifers as plotted with arrows and gradient green color bodies, respectively, which are inferred by high V_p/V_s values. Darker green color infers higher possibilities of water storage corresponding to higher V_p/V_s values.

are likely water charged, whereas the low Vp/Vs and low Vp zones where white arrows indicate in Figures 9c and 13a may be gas charged.

These zones with high water saturations mostly distribute under the valley and the NW hillslope, at distances of about larger than 130 m, which roughly coincide with the high conductivity area determined by a coincident ERT survey (Zarif et al., 2017). The inferred highest water zones roughly locate in the weathered/fractured sandstone layer at the depths of 15–30 m below topography. However, we also found that there are some gaps with relatively low Vp/Vs values where permeability should be high; thus, rocks might have become dry after groundwater flows away. If we connect intermittent high Vp/Vs zones, we interpret the possible groundwater flow path from the NW hillslope to the valley direction. Also, we connect intermittent high Vp/Vs areas at top surface and interpret them as surface water flow paths. Our results on inferring two water tables at Garner Run site (as indicated in Figure 13b) is in accordance with the observation of two water paths from distinct chemical signatures of water isotopes and solute concentrations (Li et al., 2018). The inferred groundwater flow path is likely about at depths of 20–30 m below surface, which is similar to the borehole evidence for groundwater depths at the nearby Shale Hills (Gu et al., 2020). The possible water aquifers are depicted with gradient green color, where darker green color infers higher possibilities of water storage corresponding to higher Vp/Vs values. The inferred water aquifers are mainly in the middle layer with weathered/fractured bedrock. Moreover, future work will include quantitative interpretation of EFWI Vp and Vs models with reference of a rock physics model (Mavko et al., 2009) to simultaneously quantify subsurface porosity and water saturation/content.

4. Conclusions

We have proposed effective EFWI strategies to image CZ heterogeneities. Specific to noisy near-surface vertical-component geophone data, we implement EFWI with windowed early-arrival refractions. To remove the interferences of unreliable amplitudes, which mainly occur along offsets for windowed refraction data, we propose to use the correlative based misfit instead of the classic L_2 misfit in EFWI. Compared to the L_2 misfit, the correlative misfit based EFWI produces more structural details by balancing amplitudes between near and far offsets. Furthermore, in case of incomplete propagation physics with the example of unknown densities, the correlative misfit ensures more stable inversion for Vp and Vs models, and the hybrid TV and Tikhonov regularization term suppresses random noise and improves the inversion robustness. Following validation experiments with synthetic data, we apply our EFWI method with the regularized correlative misfit to the field data collected at the Garner Run site of SSHCZO. With the constraint of $Vp/Vs > 1$, EFWI is able to update Vp and Vs models with high-resolution details, in particular highlighting three distinguished layers and low Vp and Vs zones. Based on the theory of fluid substitution that high and low Vp/Vs values refer to possible water and gas saturation, respectively, we depict possible gas and water saturated zones. Moreover, two water tables with the surface and the underground water flow paths can be inferred at the Garner Run site. In this application, we have demonstrated that the proposed EFWI method designed for processing seismic refraction data is robust for estimating high-resolution Vp and Vs models from poor initial models only using noisy single component data. We believe that it is ready for broad applications beyond the Garner Run site to process other seismic refraction datasets.

Data Availability Statement

Seismic refraction data in Garner Run is available at <http://www.hydroshare.org/resource/759a4482482647ecbc164f6bcf1eb157>. The further processed data with SU (Seismic Unix) header are available at <https://zenodo.org/record/5813185#.YeBe1rj0mUk>.

References

- Adamczyk, A., Malinowski, M., & Malehmir, A. (2014). High-resolution near-surface velocity model building using full-waveform inversion—A case study from southwest Sweden. *Geophysical Journal International*, 197(5), 1693–1704. <https://doi.org/10.1093/gji/ggu070>
- Athanasopoulos, N., Manukyan, E., Bohlen, T., & Maurer, H. (2020). Time–frequency windowing in multiparameter elastic FWI of shallow seismic wavefield. *Geophysical Journal International*, 222, 1164–1177. <https://doi.org/10.1093/gji/ggaa242>
- Befus, K., Sheehan, A., Leopold, M., Anderson, S., & Anderson, R. S. (2011). Seismic constraints on critical zone architecture, Boulder Creek watershed, Front Range, Colorado. *Vadose Zone Journal*, 10, 915–927. <https://doi.org/10.2136/vzj2010.0108>
- Bozdağ, E., Peter, D., Lefebvre, M., Komatitsch, D., Tromp, J., Hill, J., et al. (2016). Global adjoint tomography: First-generation model. *Geophysical Journal International*, 207, 1739–1766.

Acknowledgments

The research is funded by the NSF Grant EAR 1919650. Logistical support and referenced geospatial data were provided by the NSF-supported Shale Hills Susquehanna Critical Zone Observatory. The authors thank the helpful discussion with Chao Huang on seismic data processing.

- Bunks, C., Salek, F. M., Zaleski, S., & Chavent, G. (1995). Multiscale seismic waveform inversion. *Geophysics*, *60*, 1457–1473. <https://doi.org/10.1190/1.1443880>
- Chen, P., Zhao, L., & Jordan, T. H. (2007). Full 3D tomography for the crustal structure of the Los Angeles region. *Bulletin of the Seismological Society of America*, *97*(4), 1094–1120. <https://doi.org/10.1785/0120060222>
- Chi, B., Dong, L., & Liu, Y. (2015). Correlation-based reflection full-waveform inversion. *Geophysics*, *80*(4), R189–R202. <https://doi.org/10.1190/geo2014-0345.1>
- Choi, Y., & Alkhalifah, T. (2012). Application of multi-source waveform inversion to marine streamer data using the global correlation norm. *Geophysical Prospecting*, *60*, 748–758. <https://doi.org/10.1111/j.1365-2478.2012.01079.x>
- Del Vecchio, J., DiBiase, R. A., Denn, A. R., Bierman, P. R., Caffee, M. W., & Zimmerman, S. R. (2018). Record of coupled hillslope and channel response to Pleistocene erosion and deposition in a sandstone headwater valley, central Pennsylvania. *Bulletin*, *130*(11–12), 1903–1917. <https://doi.org/10.1130/b31912.1>
- Flinchum, B. A., Steven Holbrook, W., Rempe, D., Moon, S., Riebe, C. S., Carr, B. J., et al. (2018). Critical zone structure under a granite ridge inferred from drilling and three-dimensional seismic refraction data. *Journal of Geophysical Research: Earth Surface*, *123*(6), 1317–1343. <https://doi.org/10.1029/2017jf004280>
- Gao, F., Levander, A. R., Pratt, R. G., Zelt, C. A., & Fradelizio, G. L. (2006). Waveform tomography at a groundwater contamination site: VSP-surface data set. *Geophysics*, *71*, H1–H11. <https://doi.org/10.1190/1.2159049>
- Gao, K., & Huang, L. (2019). Acoustic- and elastic-waveform inversion with total generalized p-variation regularization. *Geophysical Journal International*, *218*(2), 933–957. <https://doi.org/10.1093/gji/ggz203>
- Gardner, G. H. F., Gardner, L. W., & Gregory, A. R. (1974). Formation velocity and density—the diagnostic basics for stratigraphic traps. *Geophysics*, *39*(6), 770–780. <https://doi.org/10.1190/1.1440465>
- Goldstein, T., & Osher, S. (2009). The split Bregman method for L1-regularized problems. *SIAM Journal on Imaging Science*, *2*(2), 323–343. <https://doi.org/10.1137/080725891>
- Górszczyk, A., Brossier, R., & Métivier, L. (2021). Graph-space optimal transport concept for timedomain full-waveform inversion of ocean-bottom seismometer data: Nankai Trough velocity structure reconstructed from a 1D model. *Journal of Geophysical Research: Solid Earth*, *126*, e2020JB021504.
- Gu, X., Mavko, G., Ma, L., Oakley, D., Accardo, N., Carr, B. J., et al. (2020). Seismic refraction tracks porosity generation and possible CO₂ production at depth under a headwater catchment. *Proceedings of the National Academy of Sciences*, *117*(32), 18991–18997. <https://doi.org/10.1073/pnas.2003451117>
- Hayes, J. (2019). *SSHczo -- Geophysics, seismic refraction, geomorphology -- Garner Run. (Sandstone Forested) -- (2016-2017)*, HydroShare Retrieved from <http://www.hydroshare.org/resource/759a4482482647ecbc164f6bcf1eb157>
- Hayes, J. L., Riebe, C. S., Holbrook, W. S., Flinchum, B. A., & Hartsough, P. C. (2019). Porosity production in weathered rock: Where volumetric strain dominates over chemical mass loss. *Science Advances*, *5*(9), eaao0834. <https://doi.org/10.1126/sciadv.aao0834>
- Holbrook, W. S., Riebe, C. S., Elwaseif, M., Hayes, L. J., Basler-Reeder, K., Harry, L., et al. (2014). Geophysical constraints on deep weathering and water storage potential in the Southern Sierra Critical Zone Observatory. *Earth Surface Processes and Landforms*, *39*(3), 366–380. <https://doi.org/10.1002/esp.3502>
- Huang, C., & Zhu, T. (2020). Towards real-time monitoring: Data assimilated time-lapse full waveform inversion for seismic velocity and uncertainty estimation. *Geophysical Journal International*, *223*(2), 811–824. <https://doi.org/10.1093/gji/ggaa337>
- Huang, C., Zhu, T., & Hayes, L. J. (2019). *Seismic full waveform inversion procedure for characterizing critical zone subsurface structure: A case study at the Susquehanna Shale Hills Critical Zone Observatory*. AGU Fall Meeting Abstracts, NS23A-01.
- Kamei, R., Pratt, R. G., & Tsuji, T. (2012). Waveform tomography imaging of a megasplay fault system in the seismogenic Nankai subduction zone. *Earth and Planetary Science Letters*, *317–318*, 343–353. <https://doi.org/10.1016/j.epsl.2011.10.042>
- Köhn, D., Nil, D., Kurzman, A., Przebindowska, A., & Bohlen, T. (2012). On the influence of model parameterization in elastic full waveform tomography. *Geophysical Journal International*, *191*, 325–345.
- Lailly, P. (1983). The seismic inverse problem as a sequence of before stack migrations. In J. B. Bednar, R. Redner, E. Robinson, & A. Weglein (Eds.), *Conference on inverse scattering: Theory and application*. SIAM, 206–220.
- Li, L., DiBiase, R. A., Del Vecchio, J., Marcon, V., Hoagland, B., Xiao, D., & Brantley, S. L. (2018). The effect of lithology and agriculture at the Susquehanna Shale Hills Critical Zone Observatory. *Vadose Zone Journal*, *17*(1), 1–15. <https://doi.org/10.2136/vzj2018.03.0063>
- Lin, Y., & Huang, L. (2015). Acoustic- and elastic-waveform inversion using a modified total-variation regularization scheme. *Geophysical Journal International*, *200*, 489–502.
- Liu, Q., & Peter, D. (2020). Square-Root Variable Metric-Based Nullspace Shuttle: A Characterization of the Nonuniqueness in Elastic Full-Waveform Inversion. *Journal of Geophysical Research: Solid Earth*, *125*(2), e2019JB018687.
- Liu, Y., He, B., Lu, H., Zhang, Z., Xie, X. B., & Zheng, Y. (2018). Full-intensity waveform inversion. *Geophysics*, *83*(6), R649–R658. <https://doi.org/10.1190/geo2017-0682.1>
- Ma, L., Oakley, D., Nyblade, A., Moon, S., Accardo, N., Wang, W., & Brantley, S. L. (2021). Seismic imaging of a Shale landscape under compression shows limited influence of topography-induced fracturing. *Geophysical Research Letters*, *48*(17), e2021GL093372. <https://doi.org/10.1029/2021gl093372>
- Mavko, G., Mukerji, T., & Dvorkin, J. (2009). *The rock physics handbook: Tools for seismic analysis of porous media*. Cambridge University Press.
- Modrak, R., & Tromp, J. (2016). Seismic waveform inversion best practices: Regional, global, and exploration best cases. *Geophysical Journal International*, *206*, 1864–1889. <https://doi.org/10.1093/gji/ggw202>
- National Research Council. (2001). *Basic research opportunities in earth science*. National Academies Press.
- Nocedal, J., & Wright, S. J. (2006). *Numerical optimization*. Springer.
- Pan, W., Innanen, K. A., Margrave, G. F., Fehler, M. C., Fang, X., & Li, J. (2016). Estimation of elastic constants for HTI media using Gauss-Newton and full-Newton multiparameter full-waveform inversion. *Geophysics*, *81*(5), R275–R291. <https://doi.org/10.1190/geo2015-0594.1>
- Parsekian, A. D., Singha, K., Minsley, B. J., Holbrook, W. S., & Slater, L. (2015). Multiscale geophysical imaging of the critical zone. *Reviews of Geophysics*, *53*(1), 1–26. <https://doi.org/10.1002/2014rg000465>
- Prieux, V., Brossier, R., Operto, S., & Virieux, J. (2013a). Multiparameter full waveform inversion of multicomponent ocean-bottom-cable data from the Valhall field. Part 1: Imaging compressional wave speed, density and attenuation. *Geophysical Journal International*, *194*(3), 1640–1664. <https://doi.org/10.1093/gji/ggt177>
- Prieux, V., Brossier, R., Operto, S., & Virieux, J. (2013b). Multiparameter full waveform inversion of multicomponent ocean-bottom-cable data from the Valhall field. Part 2: Imaging compressive-wave and shear-wave velocities. *Geophysical Journal International*, *194*(3), 1665–1681. <https://doi.org/10.1093/gji/ggt178>

- Ravasi, M., Vasconcelos, I., Curtis, A., & Kritski, A. (2015). Vector-acoustic reverse time migration of Volve ocean-bottom cable data set without up/down decomposed wavefields. *Geophysics*, *80*(4), S137–S150. <https://doi.org/10.1190/geo2014-0554.1>
- Routh, P., Krebs, J., Lazaratos, S., Baumstein, A., Lee, S., Cha, Y. H., & Anderson, J. (2011). Encoded simultaneous source full-wavefield inversion for spectrally shaped marine streamer data. In *SEG Technical Program Expanded Abstracts 2011* (pp. 2433–2438). Society of Exploration Geophysicists.
- Sheng, J., Leeds, A., Buddensiek, M., & Schuster, G. T. (2006). Early arrival waveform tomography on near-surface refraction data. *Geophysics*, *71*(4), U47–U57. <https://doi.org/10.1190/1.2210969>
- Smithyman, B., Pratt, R. G., Hayles, J., & Wittebolle, R. (2009). Detecting near-surface objects with seismic waveform tomography. *Geophysics*, *74*, WCC119–WCC127. <https://doi.org/10.1190/1.3223313>
- Tarantola, A. (1984). Inversion of seismic reflection data in the acoustic approximation. *Geophysics*, *49*, 1259–1266. <https://doi.org/10.1190/1.1441754>
- Tarantola, A. (1986). *A strategy for nonlinear elastic inversion of seismic reflection data*. In 56th Annual International Meeting, SEG, Expanded Abstracts, 1893–1903. <https://doi.org/10.1190/1.1442046>
- Vigh, D., Jiao, K., Watts, D., & Sun, D. (2014). Elastic full-waveform inversion application using multicomponent measurements of seismic data collection. *Geophysics*, *79*(2), R63–R77. <https://doi.org/10.1190/geo2013-0055.1>
- Virieux, J., & Operto, S. (2009). An overview of full-waveform inversion in exploration geophysics. *Geophysics*, *74*(6), WCC1–WCC26. <https://doi.org/10.1190/1.3238367>
- Wang, H., Burtz, O., Routh, P., Wang, D., Violet, J., Lu, R., & Lazaratos, S. (2021). Anisotropic 3D elastic full-wavefield inversion to directly estimate elastic properties and its role in interpretation. *The Leading Edge*, *40*(4), 277–286. <https://doi.org/10.1190/tle40040277.1>
- Wang, W., Nyblade, A., Mount, G., Moon, S., Chen, P., Accardo, N., & Brantley, S. L. (2021). 3D seismic anatomy of a watershed reveals climate-topography coupling that drives water flowpaths and bedrock weathering. *Journal of Geophysical Research: Earth Surface*, *126*, e2021JF006281. <https://doi.org/10.1029/2021jfo06281>
- Wang, X.-Q., Schubnel, A., Fortin, J., David, E. C., Guéguen, Y., & Ge, H.-K. (2012). High Vp/Vs ratio: Saturated cracks or anisotropy effects? *Geophysical Research Letters*, *39*, L11307. <https://doi.org/10.1029/2012gl051742>
- Wang, Y., Miller, R. D., Peterie, S. L., Sloan, S. D., Moran, M. L., Cudney, H. H., et al. (2019). Tunnel detection at Yuma proving ground, Arizona, USA – Part 1: 2D full-waveform inversion experiment. *Geophysics*, *84*, B95–B105. <https://doi.org/10.1190/geo2018-0598.1>
- Zarif, F., Kessouri, P., & Slater, L. (2017). Recommendations for field-scale induced polarization (IP) data acquisition and interpretation. *Journal of Environmental & Engineering Geophysics*, *22*(4), 395–410. <https://doi.org/10.2113/jee22.4.395>